

---

ELEVENTH SYMPOSIUM ON

# turbulent shear flows

---

Grenoble, France  
September 8-10, 1997

**DISTRIBUTION STATEMENT A**

Approved for public release;  
Distribution Unlimited

DTIC QUALITY INSPECTED 4

LATE PAPERS

19971209 081



**ELEVENTH SYMPOSIUM ON TURBULENT SHEAR FLOWS**  
**Institut National Polytechnique**  
**Université Joseph Fourier**  
**Grenoble, September 8-10, 1997**

**LATE PAPERS**

- |   |      |
|---|------|
| Low dimensional description of large scale structures dynamics in a plane turbulent mixing layer<br><i>L. Cordier, J. Delville, C. Tenaud</i> | L-1  |
| Simulation of coherent structures in variable density coaxial jets<br><i>P. Reynier, A. Kourta, H. Ha Minh</i>                                | L-7  |
| Amplification and reduction of turbulence in a heated jet/shock wave interaction<br><i>L. Jacquin, P. Geffroy</i>                             | L-12 |

# LOW-DIMENSIONAL DESCRIPTION OF LARGE SCALE STRUCTURE DYNAMICS IN A PLANE TURBULENT MIXING LAYER.

L. CORDIER<sup>(1)</sup>, J. DELVILLE<sup>(1)</sup> and C. TENAUD<sup>(2)</sup>

<sup>(1)</sup> L.E.A. / C.E.A.T. - UMR CNRS 6609  
43, Route de l'Aérodrome, 86036 POITIERS CEDEX, FRANCE

<sup>(2)</sup> L.I.M.S.I. - UPR CNRS 3251  
B.P. 133, 91403 ORSAY CEDEX, FRANCE

## INTRODUCTION

The active control of fully developed turbulent flows are of particular interest for many industrial applications. In fact, as regards aerodynamic applications, the control and modification of turbulent flows could be used either in external flows, to reduce the total drag of aerospace vehicles or in internal flows, to increase the mixing rate in a scram-jet for instance. However, as these industrial applications are complex, we limit the present study to the analysis of a basic free turbulent flow: the incompressible, turbulent mixing layer developing spatially downstream a flat plate.

In such a flow field, large-scale coherent structures exist which contain most of the turbulent kinetic energy. These coherent structures are mainly responsible for vibrations, noise generation, etc... Therefore, in term of control, it seems important to describe correctly the characteristics of these structures and to predict precisely their time evolution using models as simple as possible. One of the methods proposed to mimic the dynamical behaviour of the flow is to develop a low-order dynamical system. This study presents the ability of the Proper Orthogonal Decomposition (POD) (Lumley, 1967) to obtain this low-order dynamical system. In the POD approach, the coherent structures are defined in terms of optimal signature of the turbulent kinetic energy. The coherent structures are then associated to the eigenfunctions of the POD. This method has already been used, with success, to study either the near-wall evolution of the flow within a turbulent boundary layer (Aubry *et al.*, 1988) or the dynamical evolution of a jet (Corke *et al.*, 1994).

The aim of the present study is to apply such procedures on the results of the L.E.S. of a 3D, plane mixing layer spatially developing downstream of a flat plate. The L.E.S. has been performed on the flow configuration studied experimentally in details in earlier works (see Delville 1994, Ukeiley 1995, Cordier 1996, Cordier *et al.* 1997). Several gains can be derived from such a L.E.S. computation: mainly the whole flow field is known in a deterministic way, thus the efficiency of the POD can be determined and the time evolution of the POD modes studied in details. The data-base generated by this simulation can be used to check assumptions that are required when experimental

procedures are applied: mainly the pressure, experimentally difficult to obtain, can be taken into account and the feedback relations (Aubry *et al.*, 1988) between the modeled structures and the mean field can be sorted out.

We present here the results concerning the L.E.S. that has been performed. Scalar "classical" PODs and a snapshot-POD are derived from these numerical results. It is shown that the spatial eigenfunctions are in good agreement with the ones obtained experimentally. Endly a low-order dynamical system is derived. The random coefficients obtained from the dynamical system and the ones directly calculated from the L.E.S. results are compared.

## THE SNAPSHOT-POD METHOD

In order to analyze the organization present in the mixing layer, the Snapshot-POD method (Sirovich, 1987) is applied on the numerical results given from the L.E.S.. This method based on spatial averaged quantities, has been preferred to the "standard" approach (Lumley 1967), since simulations use an important number of grid points but rather limited temporal samples compared to experiments.

### Basic approach:

Every spatio-temporal event  $\underline{v}_i(\underline{x}, t)$  is decomposed using a mean and a fluctuating parts:

$$\underline{v}_i(\underline{x}, t) = \overline{\underline{v}_i}(\underline{x}) + \underline{v}'_i(\underline{x}, t) \quad (1)$$

where the mean part is expressed with an average in time:

$$\overline{\underline{v}_i}(\underline{x}) = \frac{1}{T} \int_T \underline{v}_i(\underline{x}, t) dt$$

The fluctuating quantities can be written using a discrete basis of the flow:

$$\underline{v}'_i(\underline{x}, t) = \sum_{n=1}^{N_{POD}} A^{(n)}(t) \underline{\Phi}_i^{(n)}(\underline{x}) \quad (2)$$

where  $N_{POD}$  is the number of modes solved in the POD. In the snapshot-POD approach, the purely temporal eigen-

functions ( $A^{(n)}(t)$ ) are calculated by means of a Fredholm integral equation:

$$\int_T C(t, t') A^{(n)}(t') dt' = \Lambda^{(n)} A^{(n)}(t) \quad (3)$$

where  $C(t, t')$  is the temporal velocity-correlations:

$$\begin{aligned} C(t, t') &= \frac{1}{T} \int_{\mathcal{D}} \underline{v}_i(\underline{x}, t) \underline{v}_i'(\underline{x}, t') d\underline{x} \\ &= \frac{1}{T} \sum_{n=1}^{N_{POD}} A^{(n)}(t) A^{(n)}(t') \end{aligned} \quad (4)$$

and where  $\Lambda^{(n)}$  are the (real, positive) eigenvalues of this tensor. Each eigenvalue is associated to the energy density contained in the corresponding mode and the sum of  $\Lambda^{(n)}$  is equal to the turbulent kinetic energy included in the integral domain ( $\mathcal{D}$ ). The spatial eigenfunctions are then deduced from:

$$\Phi_i^{(n)}(\underline{x}) = \frac{1}{T \Lambda^{(n)}} \int_T \underline{v}_i(\underline{x}, t) A^{(n)}(t) dt \quad (5)$$

### Data Compression: "scalar-POD approach"

In order to reduce the data storage requirements, a data compression procedure is used. This compression is based on a scalar version of the "classical" POD introduced by Lumley (1967). We retain only "relevant" modes of this decomposition to rebuild the flow realizations that are used in the snapshot-POD analysis. In this approach, we express each component of velocity of the flow realizations in terms of spatial eigen-functions depending only on the  $x$  and  $y$  directions:

$$\tilde{\underline{v}}_i(\underline{x}, t) = \sum_{n=1}^{N^*} a_i^{(n)}(z, t) \varphi_i^{(n)}(x, y) \quad (6)$$

where:

$$\underline{v}_i(\underline{x}, t) = \langle \underline{v}_i \rangle(x, y) + \tilde{\underline{v}}_i(\underline{x}, t) \quad (7)$$

and

$$\langle \underline{v}_i \rangle(x, y) = \frac{1}{T} \int_T \int_{L_z} \underline{v}_i(x, y, z, t) dt dz.$$

For this scalar POD, the integral Fredholm problem which is solved is<sup>1</sup>

$$\int_{L_x} \int_{L_y} R_{\alpha\alpha}(x, y, x', y') \varphi_{\alpha}^{(n)}(x', y') dx' dy' = \lambda^{(n)} \varphi_{\alpha}^{(n)}(x, y) \quad (8)$$

By this way, instead of storing  $3 \times N_x \times N_y \times N_z \times N_t$  floating point numbers, we just need to store  $3 \times N_x \times N_t \times N^{KL}$  numbers to describe the temporal history of the 3D flow field. Here among the  $N^* = N_x \times N_y$  modes resulting from each of the scalar PODs, only  $N^{KL}$  modes are retained.  $N^{KL}$  is the Karhunen-Loeve dimension of the scalar PODs, i.e. the minimum number of modes necessary to rebuild the turbulent energy with an accuracy better than 99%.

In practice, the velocity correlations ( $R_{ii}(x, y, x', y')$ ) are calculated from the L.E.S. results using the following relationship:

$$\begin{aligned} R_{ii}(x, y, x', y') &= \langle \underline{v}_i \cdot \underline{v}_i \rangle(x, y, x', y') \\ &= \langle \underline{v}_i \rangle(x, y) \cdot \langle \underline{v}_i \rangle(x', y') \end{aligned} \quad (9)$$

<sup>1</sup>No implicit summation over greek subscripts.

The space-time coefficients ( $a_i^{(n)}(z, t)$ ) are then evaluated by projection:

$$a_i^{(n)}(z, t) = \int_{L_x} \int_{L_y} \tilde{\underline{v}}_i(x, y, z, t) \cdot \varphi_i^{(n)}(x, y) dx dy \quad (10)$$

and verify the orthogonality relationship:

$$\frac{1}{L_z T} \int_T \int_{L_z} a_i^{(n)}(z, t) \cdot a_i^{(m)}(z, t) dz dt = \lambda_i^{(n)} \delta_{nm}$$

## VALIDATION OF THE L.E.S. RESULTS

### Large Eddy Simulation:

The L.E.S. of the mixing layer is performed using the filtered Navier-Stokes equations written in the velocity-vorticity formulation, by means of the Reynolds decomposition (Lardat *et al.*, 1997). In order to take into account the participation of the small-scale structures in the fluid motion, the subgrid scale quantities are modeled using the vorticity transfer theory of Taylor (1932), by means of an eddy viscosity expressed using the *mixed-scale model* (Ta Phuoc 1994, Sagaut 1995, Lardat *et al.* 1997).

The spatial discretization, based on a finite difference method, uses a M.A.C. staggered grid. The system of equations is solved in two steps (Lardat *et al.*, 1997). First we solve the transport equation of the vorticity by means of a Crank-Nicholson, Adams-Bashforth approximation and a QUICK scheme. Secondly, knowing the new vorticity field, the velocity is solved using a projection (or fractional step) method, following the work made by Bertagnolio and Daube (1996). Let us mention that this scheme is  $2^{nd}$  order accurate in both time and space.

The L.E.S. is performed on the same flow configuration as the experimental one obtained by Delville (1995). The velocity ratio is  $r = U_2/U_1 = 0.59$ , where  $U_1 = 42.8$  m/s and  $U_2 = 25.2$  m/s are the magnitudes of the external velocities of the boundary layers at the trailing edge of the flat plate. The Reynolds number, based on  $\delta_{\omega_0}$  and on  $\Delta U = U_1 - U_2$ , is 35000 ( $\delta_{\omega_0}$  refers to the experimental vorticity thickness at a prescribed location,  $\delta_{\omega_0} = 30 \times 10^{-3}$  m). The computational domain starts at the trailing edge of the flat plate. It spreads over  $20 \delta_{\omega_0}$  in the streamwise direction,  $6 \delta_{\omega_0}$  in the inhomogeneous (vertical) direction ( $y$ ) and lays over  $5 \delta_{\omega_0}$  in the spanwise direction ( $z$ ).

The grid uses  $401 \times 71 \times 55$  nodes in the  $x \times y \times z$  directions and is tightened around the centerline of the mixing layer in the inhomogeneous direction ( $y$ ). The flow is supposed to be periodic in the spanwise direction ( $z$ ). Using this mesh, the grid filter width ( $\overline{\Delta} = (\Delta x \times \Delta y \times \Delta z)^{1/3}$ ) is close to the Taylor micro-scale estimated following the experimental results (Delville, 1995).

As regards the boundary conditions at the inflow surface (ie. the trailing edge of the splitting plate), the normal component of the mean velocity is initialized using two turbulent Whitfield profiles for the boundary layers from each side of the flat plate. The profiles of the tangential components of the mean vorticity are then deduced from the velocity profiles. A white noise is superimposed on the tangential components of the mean vorticity. The perturbation magnitude is equivalent to an amplitude of  $10^{-3} U_1$  on the streamwise velocity component. At the outlet boundary ( $x = 20 \delta_{\omega_0}$ ), the tangential components of the vorticity are calculated by extrapolation along the characteristics. The normal component of the velocity is then deduced from the vorticity profiles, prescribing that the mass conservation is satisfied. At the upper and lower surfaces of the domain ( $y = \pm 3 \delta_{\omega_0}$ ), slip conditions are imposed (Lardat *et al.*, 1997).

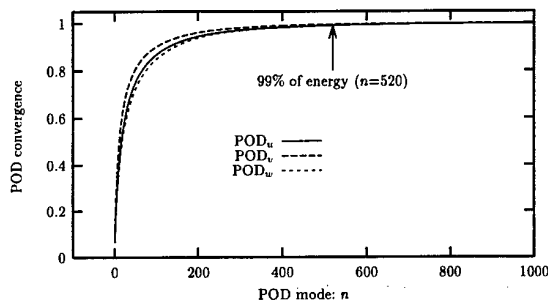


Figure 1: Energy contained in the first  $n$  modes of the scalar-PODs.

To compare the numerical results with the experimental data, a portion of the computational domain has been selected. This region starts from  $5 \delta_{\omega_0}$  downstream of the trailing edge of the flat plate and lays over  $10 \delta_{\omega_0}$  to minimize the influence of the exit boundary condition.

### Validations of the Simulation:

A comparison of the numerical results has been performed with the experimental data on the mean and Reynolds stress profiles. The self-similarity behavior of the mixing layer is recovered by the L.E.S.; the vorticity thickness ( $\delta_\omega$ ) and its longitudinal evolution ( $d\delta_\omega/dx$ ) are correctly predicted by the computation (L.E.S.:  $d\delta_\omega/dx = 4.22 \cdot 10^{-2}$ ; Experiments:  $d\delta_\omega/dx = 4.1 \cdot 10^{-2}$ ). Very good agreements are achieved on the profiles of the Reynolds stress component (Lardat *et al.*, 1997). As regards the organization of the mixing layer, the large scale arrangement strongly tridimensionnal, is well predicted. In fact, the spatial length scales recorded are close to  $\eta_x \sim 3.25 \delta_\omega$  in the streamwise direction ( $x$ ) and  $\eta_z \sim 2/3 \eta_x$  in the spanwise direction ( $z$ ) which are in rather good agreement with the ones generally admitted (see Bernal and Roshko, 1986).

### Application of the Scalar-PODs:

The scalar-POD approaches are applied on the fluctuating velocity  $\tilde{u}_i$  field provided by the numerical simulation. The POD analysis is performed on 1000 temporal events representing a dimensionless time close to  $T = 17$ . We apply the POD on a box with a streamwise extent of  $10\delta_{\omega_0}$ . In practice, knowing an initial state, we have first run the calculation on 1000 time steps to calculate the spatial velocity correlations ( $R_{ii}(x, y, x', y')$ ) (9). Secondly, the eigenvalue-eigenfunction problem (8) have been solved. Finally, the simulation have been re-run from the same previous initial state to calculate the space-time coefficients ( $a_i^{(n)}(z, t)$ ) (10).

The convergence of the scalar-PODs is presented on the ratio  $\sum_{i=1}^n \lambda^{(i)} / \sum_{i=1}^{N^*} \lambda^{(i)}$  between the energy contained in the first  $n$ -POD modes and the turbulent kinetic energy in the flow (Fig. 1). The convergence is relatively rapid since about 57 % of the turbulent kinetic energy is contained within the 20 first modes and the first 520 modes contain 99 % of the turbulent kinetic energy. One can note that a large compression ratio (90%) is obtained;  $N_x N_y / N^* \simeq 10$ .

Iso-contours of  $\varphi_i^{(n)}(x, y)$  are presented in Fig 2 for four selected modes (modes 1, 2, 20 and 200) in the plane ( $x, y$ ). In these figures, the lines in bold correspond to positive values while the thin ones correspond to negative ones. Considering these eigenfunctions, one can notice a streamwise shift when comparing modes 1 and 2. Whatever the velocity components are, the mode 2 is shifted downstream

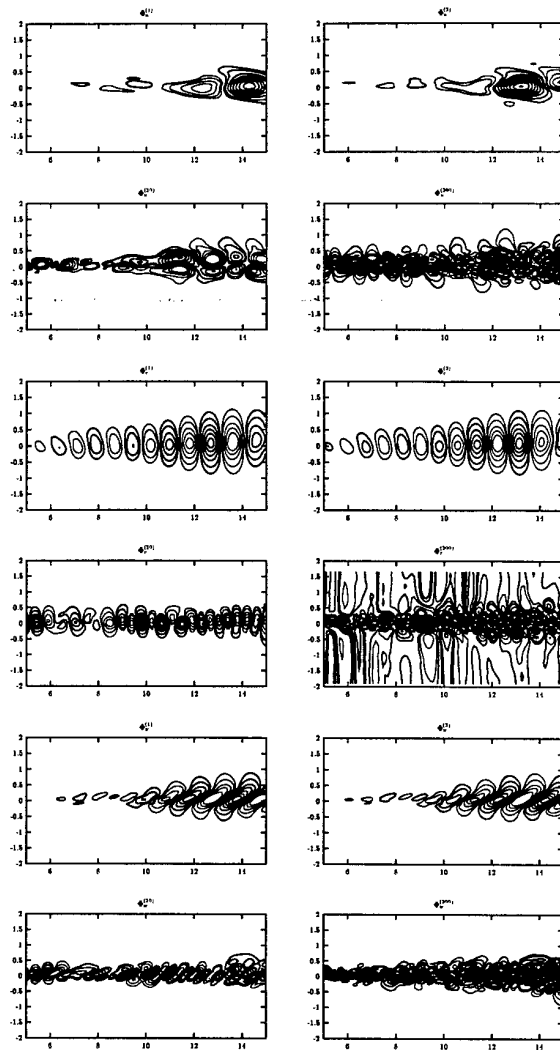


Figure 2: Iso-contours of the spatial eigenfunctions from the scalar-PODs of the three components of the velocity ( $u, v, w$ ) for modes 1, 2, 20 and 200 (from top to bottom).

when compared to mode 1. This behaviour is due to the convective nature of the flow (Rempfer, 1993). In fact the first two modes of the POD have to be considered simultaneously if one wants to represent the mean convection in the streamwise direction. All these eigenfunctions exhibit a preferred organization; for low-order modes, this organization follows the longitudinal expansion of the mixing layer which is noticeable on Fig. 2. However, compared to these low-order modes, the high-order modes are more tightened in the vicinity of the centerline of the mixing layer and correspond to smaller spatial length scales.

The temporal evolution of the first four random coefficients for the scalar PODs are plotted Fig. 3, for the three scalar functions ( $u, v, w$ ), on the middle  $z$ -plane ( $z = z_0$ ). A time shift is visible between  $a^{(1)}(z_0, t)$  and  $a^{(2)}(z_0, t)$  and between  $a^{(3)}(z_0, t)$  and  $a^{(4)}(z_0, t)$ , which is also due to the convective nature of the flow (Rempfer, 1993).

The good agreement between the computations and experiments can also be shown when the two-point space correlations  $R_{ii}(x_0, y_0, x', y')$  are considered. From the scalar-

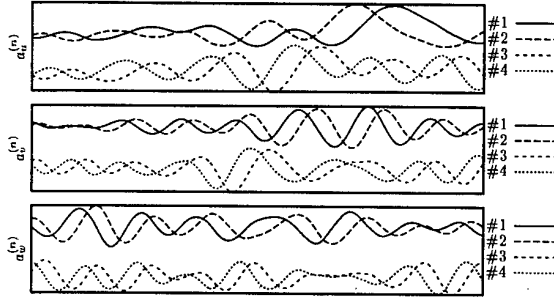


Figure 3: Temporal evolution of the eigenfunctions of the 4 first modes of the scalar-PODs.

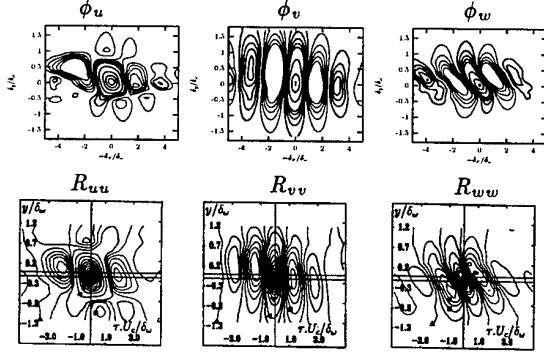


Figure 4: Comparison in a plane  $(\tau, y)$  or  $(-x, y)$  of the experimentally measured space time correlations  $R_{ii}(\tau; y, y')$  (bottom) with the space correlations obtained from the contribution of the first 200 modes of the scalar PODs from the L.E.S. (top)

POD, this correlation can be written:

$$R_{ii}(x_0, y_0, x', y') \propto \sum_{n=1}^{N^*} \lambda^{(n)} \varphi_i^{(n)}(x_0, y_0) \varphi_i^{(n)}(x', y')$$

In order to validate the eigenfunctions, they can be compared to the space-time correlations experimentally determined by using Taylor hypothesis as in Delville (1995). On figure 4, the space-time correlations experimentally measured are compared to the contribution of the first 200 POD modes to the spatial correlations. On these figures, the reference point  $(x_0, y_0)$  is located at the center of the selected spatial domain. Very good agreements are achieved. We must underline that the overall shape of the measured correlations is also well described by considering only few first POD modes. This comparison cross-validates computations as well as experiments. Note that the  $u$  component can be described by fluctuations of opposite sign from part to part of the mixing layer, while the  $v$  component can be described by fluctuations in phase all over the  $y$  direction, alternated in sign in the  $x$  direction (Fig. 4). Moreover, the shape of the  $w$  component indicates the presence of a strong organization for the streamwise vorticity component, this organization being recovered from both experiments and L.E.S.

#### Application of the Snapshot-POD:

The snapshot-POD method is then applied on the filtered velocity field provided by the scalar-PODs on the first  $N^{KL}$  modes. The convergence of the snapshot-POD is plotted on Fig. 5, in the same way as Fig. 1. The convergence is also very rapid since 99 % of the turbulent kinetic

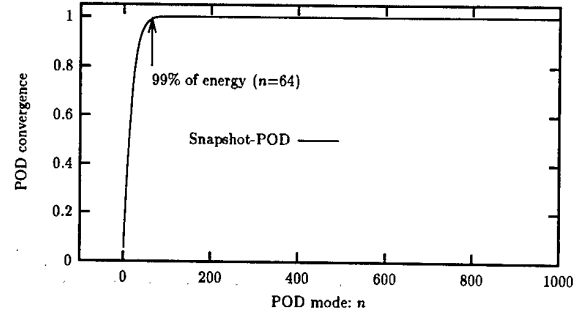


Figure 5: Energy contained in the first  $n$  modes of the snapshot POD.

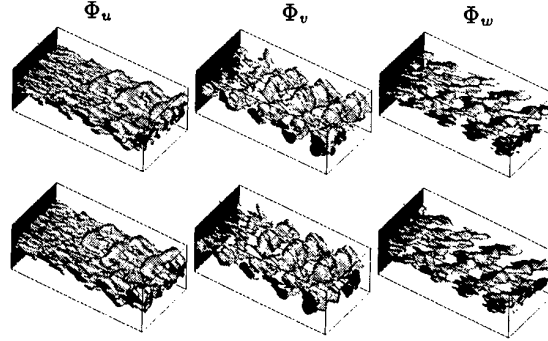


Figure 6: Iso-surface of the spatial eigenfunctions of the three components of the velocity for modes 1 (top) and 2 (bottom).

energy is contained within the 64 first modes. However, while the Karhunen-Loeve dimension seems lower in this snapshot POD, the relative number of modes required to contain 99% of energy ( $N^{KL}/N^*=0.064$ ) remains of the same order of magnitude than in the scalar POD cases ( $N^{KL}/N^*=0.1$ ).

It is notable that these eigenvalues occur in pair of almost equal values, whereas there is a gap in magnitude between these pairs. The eigenvalue problem (3) is near degenerated. To understand the consequence of this result we present in Fig. 6 positive iso-surfaces of  $\Phi_i^{(n)}(x, y, z)$  for the first two modes. Several general features can be noticed when considering these eigenfunctions. Whatever the velocity components are, one can notice a streamwise shift when comparing modes 1 and 2. It can be seen that, essentially, the eigenfunctions of this pair are representing the same structure, one of them just being shifted with respect to the other in the streamwise direction. The corresponding expansion coefficients  $A^{(1)}(t)$  and  $A^{(2)}(t)$ , are found to be analogously phase shifted in time. Hence, if we multiply each of the eigenfunctions of such a pair by its corresponding expansion coefficient, we get a structure that is moving in the streamwise direction. Analogous behavior is observed for the first higher modes and this behavior is comparable to the one already noticed in the scalar-PODs spatial modes (Fig. 2). Moreover, these eigenfunctions exhibit a preferred organization in the spanwise direction. Particularly,  $\Phi_u^{(n)}(x)$  is clearly aligned in the spanwise direction and  $\Phi_w^{(n)}(x)$  exhibits lambda-shape like structures (Fig. 6). These behaviors are similar to those observed in the analysis of the experimental data by Delville (1994).

## LOW-ORDER DYNAMICAL SYSTEM

The goal sought after, is to study the temporal behaviour of the large scale coherent structures. Therefore, the temporal approach followed previously by Aubry *et al.* (1988) and Glauser *et al.* (1989) has been employed.

### Low-dimensional model using POD:

As the pressure field is provided by the numerical simulations, a low-order dynamical system is developed by considering the Navier-Stokes equations written in pressure-velocity formulation:

$$\begin{aligned} \nabla \cdot \underline{V} &= 0 \\ \frac{\partial \underline{V}}{\partial t} + \underline{V} \cdot \nabla \underline{V} &= -\nabla P + \frac{1}{Re} \Delta \underline{V} \end{aligned} \quad (11)$$

The velocity ( $\underline{V}$ ) and the pressure ( $P$ ) are decomposed using the Reynolds decomposition (1). The velocity fluctuating part is then written using a discrete basis of the flow following equation (2). This decomposition is introduced in the transport equations (11) which are then projected onto the spatial eigenfunctions  $\underline{\Phi}^{(n)}(\underline{x})$  by means of a Galerkin projection. Since the eigenfunctions are orthogonal, a set of  $N_{gal}$  time dependent ODEs is obtained for the so-called random coefficients of the POD  $A^{(n)}(t)$ :

$$\begin{aligned} \frac{d}{dt} A^{(n)}(t) &= \sum_{m=1}^{N_{gal}} b_{nm} A^{(m)}(t) + P^{(n)}(t) \\ &+ \sum_{m=1}^{N_{gal}} \sum_{k=1}^{N_{gal}} c_{nmk} \left[ A^{(m)}(t) A^{(k)}(t) - \overline{A^{(m)}(t) A^{(k)}(t)} \right] \end{aligned} \quad (12)$$

where  $N_{gal}$  is the number of Galerkin modes retained in the dynamical system. The coefficients of the system (12)  $b_{nm}$ ,  $c_{nmk}$  are expressed as follows:

$$\begin{aligned} b_{nm} &= \left( \underline{\Phi}^{(n)}(x, y, z), \frac{1}{Re} \Delta \underline{\Phi}^{(m)}(x, y, z) \right. \\ &\quad \left. - \nabla \underline{V} \cdot \underline{\Phi}^{(m)}(x, y, z) - \nabla \underline{\Phi}^{(m)}(x, y, z) \cdot \underline{V} \right) \end{aligned}$$

$$c_{nmk} = - \left( \underline{\Phi}^{(n)}(x, y, z), \nabla \underline{\Phi}^{(m)}(x, y, z) \cdot \underline{\Phi}^{(k)}(x, y, z) \right)$$

and

$$P^{(n)}(t) = - \left( \underline{\Phi}^{(n)}(x, y, z), \nabla \tilde{P} \right) = - \int_{\partial \mathcal{D}} \tilde{P}(\underline{\Phi}^{(n)}, \underline{n}) dS$$

where  $\underline{n}$  is the external normal.

These ODEs system is solved using a 4th order Runge-Kutta integration. At the initial state, the random coefficients ( $A^{(n)}(t=0)$ ) are initialized using the projection of the events  $\underline{v}_i(\underline{x}, t)$  at  $t=0$  on the spatial eigenfunctions. We prescribe  $A^{(m)}(t) A^{(k)}(t) = \Lambda^{(m)} \delta_{mk}$  and the  $b_{nm}$  coefficients are estimated using the mean velocity given from the L.E.S.. In this first application, the pressure term contribution is neglected in a fashion comparable to Rajae *et al.* (1994).

### Results on the temporal evolution:

The dynamical system was developed on the same record than the previous results. Two sets of Galerkin modes ( $N_{gal}=10$  and  $N_{gal}=36$ ) are retained to derive two independent dynamical systems. For these numbers of mode, the relative energy contained in the system is respectively 42% and 90%. The comparisons between the random coefficients  $A^{(n)}(t)$ , obtained from the resolution of the two

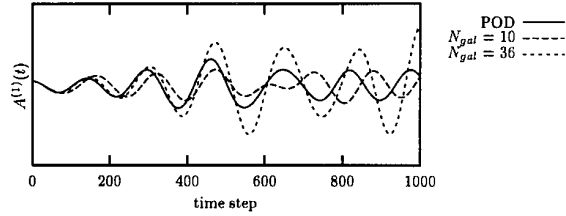


Figure 7: Comparison of the temporal evolution of the first mode for the snapshot POD and the Dynamical Systems obtained for  $N_{gal}=10$  and  $N_{gal}=36$ .

systems (12), and the projection of the events  $\underline{v}_i(\underline{x}, t)$  onto the spatial eigenfunctions  $\underline{\Phi}^{(n)}(\underline{x})$  are plotted for the first mode on the figure (7). When considering the early evolution of  $A^{(1)}(t)$  ( $t < 250$ ) both dynamical systems are able to follow the temporal evolution of this mode. The same result has been globally observed for higher modes. However, if for a short time integration, a rather good agreement is achieved, it appears that for longer time, the random coefficients  $A^{(n)}(t)$  obtained from the dynamical systems diverge from the direct POD projection. For a small truncation ( $N_{gal}=10$ ), a progressive time shift can be observed. When higher POD modes are included, this time shift can be reduced and the typical period of the modes becomes better estimated. Nevertheless, this improvement is associated with a divergence in the amplitude of the first mode. This behaviour can be explained by some of the following points. During the data compression procedure, obtained from the scalar PODs, a first truncation has been performed, therefore in some sense, a certain amount of small scales contribution has been removed from the L.E.S.. However, in projecting independently for each time step the "exact" flow field calculated from the L.E.S. on the spatial eigenfunctions, no bias is made in the estimation of the coefficients  $a^{(n)}(z, t)$ . As regards the dynamical system formulation, neglecting the pressure contribution, surely induces some inaccuracy in the model. In the same way, the instantaneous contribution of the averaged field to the dynamical system has been simplified by considering only its temporal average contribution ( $A^{(m)} A^{(k)} = \Lambda^{(m)} \delta_{mk}$ ). One last reason for the long term discrepancy can be related to the truncation done in the Galerkin projection. By taking into account additional modes (from  $N_{gal}=10$  to 36), still "energetic" modes have been added, and the system becomes relatively less dissipative. For the dynamical system ( $N_{gal}=36$ ), tests performed with additional viscosity have shown that the time-shift remains reduced, while the magnitudes of the  $A$  coefficients can be lowered.

## CONCLUSIONS

A 3D L.E.S. of the plane mixing layer have been conducted, from which the history of the 3 velocity components has been calculated on a large temporal sample. From the data base generated by this simulation, two different applications of POD have been performed. From the first POD approach, based on a scalar version of the "classical" POD, the data base has been compressed, allowing to reduce the data storage requirements of 90%. The spatial eigenfunctions  $\varphi_i^{(n)}$  mimic very well the coherent structures organization since a good agreement is achieved between their contribution to the space correlations and the correlations experimentally obtained. Using the compressed data, a 3 dimensional snapshot-POD has been performed. The spatial organization of the eigenfunctions  $\Phi_i^{(n)}$  can be favorably compared to the experimental ones.

Finally, the ability of the POD to obtain a low-order

dynamical system has been underlined. Two different dynamical systems have been performed using respectively 10 POD modes and 36 POD modes. For short time evolution, the random coefficients calculated from the dynamical systems well agree with the spatial eigenfunctions estimated from the L.E.S. results. However, for  $N_{gal}=36$ , the dynamical system are not enough dissipative. Artificial dissipation is then necessary to follow correctly the long term temporal evolution of the plane mixing layer.

These first results are very encouraging. In the near future, the influence of adding higher-order POD modes on the flow structure representation will be studied and the role of the pressure term clarified.

**Acknowledgements :** The numerical code was written by Dr R. Lardat. The authors greatly acknowledge Dr. R. Lardat and Dr. L. Ta Phuoc for their numerous and valuable comments and discussions on the numerics. The calculations have been performed on the Cray C90 of the Institut du Développement et des Ressources en Informatique Scientifique (I.D.R.I.S / C.N.R.S) Orsay, France. The authors greatly acknowledge the support of these institutions.

## REFERENCES

- Aubry N., Holmes P., Lumley J.L., & Stone E. (1988) *J. Fluid Mech.*, **192**, 115-173.
- Bernal L.P. & Roshko A. (1986) *J. Fluid Mech.*, Vol. **170**, 499-525.
- Bertagnolio F. & Daube O. (1996) "Velocity-Vorticity Formulation of the Incompressible Navier-Stokes Equations on Non Orthogonal Grids." *Proceedings of the Third ECCOMAS Computational Fluid Dynamics Conference*, pp. 644.
- Cordier L. (1996) "Etude de Systèmes Dynamiques Basés sur la Décomposition Orthogonale aux Valeurs Propres (POD) : Application à la Couche de Mélange Turbulente et à l'Écoulement Entre Deux Disques Contra-rotatifs." *Thèse de Doctorat de l'Université de Poitiers*.
- Cordier L., Manceau R., Delville J. & Bonnet J.-P. (1997) *C. R. Acad. Sci. Paris*, t. **324**, Série II b. 551-557
- Corke T.C., Glauser M.N., & Berkooz G. (1994) *Applied Mechanics Review*, **47**, N° 6, part 2, S132-S138.
- Delville J. (1994) *Applied Scientific Research* **53**, 263-281.
- Delville J. (1995) "La Décomposition Orthogonale aux Valeurs Propres et l'Analyse de l'Organisation Tridimensionnelle des Écoulements Turbulents Cisaillés Libres." *Thèse de Doctorat de l'Université de Poitiers*.
- Glauser M.N., Zheng X. & Doering C.R. (1989) "The Dynamics of Organized Structures in the Axisymmetric jet mixing layer". *Turbulence and Coherent Structures*, (eds. O. Metais and M. Lesieur), Kluwer Academic Publishers, p. 253.
- Lardat R., Bertagnolio F. & Daube O. (1997) *C. R. Acad. Sci. Paris*, t. **324**, Série II b.
- Lardat R., Dulieu A., Shen W.Z., Ta Phuoc L., Tenaud C., Cordier L. & Delville J. (1997) "Large Eddy Simulation for a Spatially Developing 3D Shear Layer in Incompressible Flow: Comparisons with detailed experiments." *Proceedings of the IUTAM Symposium on Simulation and Identification of Organized Structures in Flows*, Lyngby, Denmark.
- Lumley J.L. (1967) "The structure of inhomogeneous turbulent flows." *Atmospheric Turbulence and Radio Wave Propagation*, A.M. Yagom and V.I. Tatarski, 166-178, Moscow:Nauka.
- Rajae M., Karlsson S.K.F. & Sirovich L. (1994) *J. Fluid Mech.*, **258**, 1-29.
- Rempfer D. (1993) *Phys. Fluids*, **6**, (3), 1402-1404
- Sagaut P. (1995) "Simulations Numériques d'Écoulements Décollés avec des Modèles de Sous-maille."

*Thèse de Doctorat de l'Université PARIS VI.*

Sirovich L. (1987) *Quarterly of Applied Mathematics*, **XLV**, N° 3, 561-590.

Ta Phuoc L. (1994) "Modèles de sous maille appliqués aux écoulements instationnaires décollés." eds. DGA/DRET, *Journée thématique DRET: Aérodynamique instationnaire turbulente - Aspects numériques et expérimentaux*.

Taylor G.I. (1932) "The Transport of Vorticity and Heat through Fluids in Turbulent Motion." *Proc. of the London Math. Soc. Series A* **151**, pp 421

Ukeiley L. (1995) "Dynamics of large scale structures in a plane turbulent mixing layer" *PhD Dissertation, Clarkson Univ. NY*.



# SIMULATION OF COHERENT STRUCTURES IN VARIABLE-DENSITY COAXIAL JETS

P. Reynier, A. Kourta and H. Ha Minh

Institut de Mécanique des Fluides de Toulouse  
Avenue du Professeur Camille Soula, 31400 Toulouse, FRANCE

## ABSTRACT

This numerical investigation is devoted to the direct simulation of heterogeneous coaxial jets. The computed configuration is similar to the flow at the exit of a coaxial injector in the combustion chamber of the Vulcain rocket engine developed for Ariane V. In this flow pattern, the central jet is composed of liquid oxygen at a low speed and the annular jet is constituted of gaseous hydrogen at a higher velocity. This study is led in order to evaluate the influence of the density contrast on the pulling out of the oxygen by hydrogen for a monophasic flow. The instabilities present in the inner and outer shear-layers involve the presence of large scale vortices in the near-field. It is found that the large scale two-dimensional structures are at the origin of the destruction of the inner core. Its length is similar to this of the liquid core in the real two-phase flow. Since the breakup of the liquid jet is not easily available from experiments for this flow pattern, the simulation may improve the knowledge of the atomization process.

## INTRODUCTION

Since several years the simulation and the modelling of turbulent flows characterized by the presence of organized unsteadiness is a research theme of our team. In previous studies (see Ha Minh & Kourta 1993; Reynier & Ha Minh 1996b) turbulence models have been applied to the simulation of natural coherent structures in several flows such as the backward-facing step and the homogeneous coaxial jets. Here, the purpose is not the simulation of coherent structures using the semi-deterministic modelling (see Ha Minh & Kourta 1993) but their direct simulation. Indeed, coaxial jets are characterized by the presence of organized unsteadiness in the near-field, already observed in several experiments as those of Gladnick *et al.* (1990), Dahm *et al.* (1992) and Tang & Ko (1994). Coaxial jets play an important role in several industrial applications including cryotechnic rocket engines. This flow pattern is characterized by a complex mechanism of atomization-vaporization-combustion. As a consequence a better understanding of coaxial twin fluid atomizers is determinant to improve the performance of cryotechnic rocket engines. In this configuration the flow is a two-phase coaxial jet flow with a

central jet of liquid oxygen and an annular jet of gaseous hydrogen. This involves the presence of strong density and velocity gradients, therefore a high shearing in the inner mixing layer located at the interface between the two jets. The high shearing in the near-field is at the origin of the presence of instability waves. Generally the destruction of the liquid core is due to the generation of instabilities that initially distort and finally break the core as observed experimentally by Andrews (1993), Issac *et al.* (1994) and Mayer (1994). For Andrews (1993), the perturbations may be generated by two mechanisms: an helical wave owing to the relaxation of the velocity profile within the core and the coherent self-induction of larger perturbations from smaller ones by vortex chaining and nonlinear interaction. According to Lefebvre (1992) in liquid of low viscosity, instability waves protrude into the coflowing stream. These waves enhance the interaction between the gas and the liquid, causing the crests of the waves to detach and form ligaments, which break down into drops. As a consequence the size of the drops is directly related to the diameter of the ligaments. Other studies as those of Tsai & Viers (1992), Wu *et al.* (1992) and Wu & Faeth (1995) are in agreement with this process of drop formation. These authors reported that the formation of the drops is associated to the turbulent eddies. This process is important because it determines the initial properties of the dispersed phase, which influences mixing rates, secondary breakup, which represents the conversion of large drops into droplets, collisions and separated flow within the dispersed region (e.g. Wu *et al.* 1992). The mechanism of droplet formation is very difficult to study in cryotechnic rocket engines. According to Andrews (1993) this is due to the optical density associated to the atomization process. The investigation of Ingebo (1992) on the breakup of a cryogenic liquid jet reports that the mechanism of breakup is much more difficult to study than the atomization of fuel or water jets, because the surface temperatures were often near the boiling point of the liquid.

In the perspective of a better understanding of the breakup of the liquid core, the present paper focuses on the simulation of two-dimensional structures in heterogeneous coaxial jets for a monophasic flow. This approach

of a two-phase flow can amaze at first sight, however it is valid under certain conditions. This way is acceptable if the effects of the surface tension forces are negligible against the aerodynamic effects. In the injection of propellants at a supercritical pressure, surface tension forces play a less important role than the aerodynamic effects. Moreover, this assumption is valid at lower pressures when high gradients of density and velocity are present. This is confirmed by the experiments of Gicquel *et al.* (1995) and Lefebvre (1992) which showed that the atomization is highly dependent on both momentum and gas-liquid density ratio. In fact the flows where this approach is acceptable are the flows at high Weber numbers. This way has been applied already to the simulation of heterogeneous coaxial jets using turbulence models by Reynier & Ha Minh (1996a). These previous simulations have allowed a good prediction of the length of the liquid core which is according to Wu *et al.* (1992) of the same order that the length of the potential core in an monophase flow.

## GOVERNING EQUATIONS

This numerical study focuses on the pulling out of an heavy fluid by a lighter one under the action of the large scale structures evolving in the flow. In coaxial jets, three-dimensional effects are weak up to the end of the potential core. According to Tang & Ko (1994) in air-air coaxial jets, azimuthal structures involved by the bifurcation of two-dimensional vortices of the near region are not present before the intermediate region located downstream the end of the inner potential core. As the objective of this work is the approach of the breakup of a liquid jet, the study focuses on the near-field of the flow. Therefore, a two-dimensional approach is used for the calculations. The problem deals with coaxial jets, so the Navier-Stokes equations and the equation for the concentration rate of oxygen are solved in axisymmetric coordinates. These equations are given as:

Equation for the conservation of the density  $\rho$ :

$$\frac{\partial}{\partial t} \rho + \frac{\partial}{\partial x} \rho U + \frac{1}{r} \frac{\partial}{\partial r} r \rho V = 0 \quad (1)$$

Equation for the conservation of the momentum  $\rho U$ :

$$\begin{aligned} \frac{\partial}{\partial t} \rho U + \frac{\partial}{\partial x} \left\{ \rho U^2 + P - \mu S_{xx} \right\} \\ + \frac{1}{r} \frac{\partial}{\partial r} r \left\{ \rho UV - \mu S_{rx} \right\} = 0 \end{aligned} \quad (2)$$

Equation for the conservation of the momentum  $\rho V$ :

$$\begin{aligned} \frac{\partial}{\partial t} \rho V + \frac{\partial}{\partial x} \left\{ \rho UV - \mu S_{xr} \right\} \\ + \frac{1}{r} \frac{\partial}{\partial r} r \left\{ \rho V^2 + P - \mu S_{rr} \right\} = \frac{1}{r} \left\{ P - \mu S_{\theta\theta} \right\} \end{aligned} \quad (3)$$

The terms of the strain tensor are given by the following expressions:

$$S_{rr} = 2 \frac{\partial V}{\partial r} - \frac{2}{3} \left( \frac{\partial U}{\partial x} + \frac{\partial V}{\partial r} + \frac{V}{r} \right) \quad (4)$$

$$S_{xx} = 2 \frac{\partial U}{\partial x} - \frac{2}{3} \left( \frac{\partial U}{\partial x} + \frac{\partial V}{\partial r} + \frac{V}{r} \right) \quad (5)$$

$$S_{xr} = S_{rx} = \frac{\partial U}{\partial r} + \frac{\partial V}{\partial x} \quad (6)$$

$$S_{\theta\theta} = 2 \frac{V}{r} - \frac{2}{3} \left( \frac{\partial U}{\partial x} + \frac{\partial V}{\partial r} + \frac{V}{r} \right) \quad (7)$$

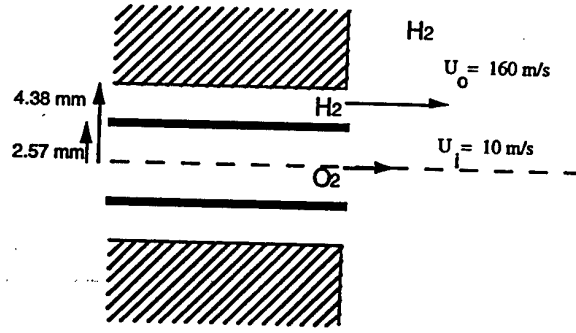


Figure 1: Computed configuration of hydrogen-oxygen coaxial jets

Equation for the conservation of the total energy  $E$ :

$$\begin{aligned} \frac{\partial}{\partial t} \rho E + \frac{\partial}{\partial x} \left\{ \left( \rho E + P - \mu S_{xx} \right) U - \mu S_{xr} V \right. \\ \left. - \gamma \left( \frac{\mu}{Pr} \right) \frac{\partial}{\partial x} e_i \right\} + \frac{1}{r} \frac{\partial}{\partial r} r \left\{ \left( \rho E + P - \mu S_{rr} \right) V \right. \\ \left. - \mu S_{xr} U - \gamma \left( \frac{\mu}{Pr} \right) \frac{\partial}{\partial r} e_i \right\} = 0 \end{aligned} \quad (8)$$

State equation for a perfect gas

$$P = (\gamma - 1) \rho e_i \quad (9)$$

Equation for the conservation of the mass fraction rate of oxygen  $\rho A$ :

$$\begin{aligned} \frac{\partial}{\partial t} \rho A + \frac{\partial}{\partial x} \left\{ \rho AU - \frac{\mu}{Sc} \frac{\partial}{\partial x} A \right\} \\ + \frac{1}{r} \frac{\partial}{\partial r} r \left\{ \rho AV - \frac{\mu}{Sc} \frac{\partial}{\partial r} A \right\} = 0 \end{aligned} \quad (10)$$

Where  $Pr$  and  $Sc$  are respectively the Prandtl and Schmidt numbers.

## NUMERICAL TOOLS

The finite-volume method proposed by MacCormack (1981) is used for the simulations. It is an implicit-explicit scheme, but to simulate the natural unsteadiness of coaxial jets only the explicit part is used in this study. The numerical scheme uses the predictor-corrector step procedure and the equations are solved under a conservative form. The method is accurate to the second order in time and space.

The flow to be computed is presented in Figure 1. It is an heterogeneous flow of oxygen and hydrogen discharging in a hydrogen atmosphere. The density ratio between the two flows is equal to 16.25. The diameter  $D$  of the injector is equal to 8.76 mm. The diameter of the central jet is 5.14 mm. The velocity  $U_i$  in the round jet is  $10 \text{ m.s}^{-1}$ , the Reynolds number is 3617 and the density  $\rho_{O_2}$  is equal to  $1.3 \text{ kg.m}^{-3}$ . The inner diameter of the annular jet is 6.74 mm and the outer diameter is 8.76 mm. The lip thickness between the two jets is 0.5 mm. The velocity  $U_o$  in the annular jet is  $160 \text{ m.s}^{-1}$  and the Reynolds number is 3880 for a density of hydrogen  $\rho_{H_2}$  equal to  $0.08 \text{ kg.m}^{-3}$ . The exit temperature is  $300^\circ \text{K}$ , the pressure  $P_e$  at the nozzle and in the computational field is initially equal to one atmosphere.

The computational domain extends over 22 diameters in the streamwise direction and 6.8 diameters in the radial direction. The grid is  $158 \times 97$ . Along  $x$ , the mesh is thin and uniform with 140 cells up to 12 diameters then coarser

up to  $22D$ . In the radial direction the grid uses a stretching outside the flow.

At the nozzle, the velocity profile has been calculated with the same numerical code which has been adapted to the simulation of a flow in a pipe. In the rest of the inlet section a wall is present (see Figure 1) then homogeneous Dirichlet conditions are applied to velocity and homogeneous Neumann conditions are imposed for concentration rate, pressure and density. As the upper boundary is far from the flow homogeneous Neumann conditions are applied for all quantities. The lower boundary is located on the flow axis, then symmetry conditions are applied. The outlet conditions are deduced from the characteristic relationships. These boundary conditions are non-reflective and have been originally developed by Thompson (1987) for the resolution of the Euler equations.

## RESULTS

In Figure 2 and 3 the profiles of the streamwise and radial velocities are presented for four sections of the flow located at  $0.25D$ ,  $1D$ ,  $3D$  and  $8D$  for the streamwise velocity and  $0.25D$ ,  $1D$ ,  $2D$  and  $8D$  for the radial velocity. The results have been averaged over 110000 time steps. The profiles of the streamwise velocity show a strong decrease of the velocity in the annular flow near the nozzle. At  $0.25D$  the velocity is equal to 45 per cent of the exit velocity. This decrease can be explained by the strong contrasts of density and velocity between the two flows. As the hydrogen flow carries filaments of oxygen, there is a high transfer of momentum from the hydrogen to the oxygen. This is supported by the profiles of the radial velocity (see Figure 3) which establish the existence of a high level of radial velocity at  $0.25D$ . Downstream, the profiles of the longitudinal velocity become flat and at  $8D$  the maximum is located on the axis. The time-averaged profiles of the spanwise velocity put in evidence a strong decrease of this quantity between  $0.25D$  and  $1D$ . Next this location the time-averaged level of the radial velocity is weak.

The unsteady field of the mass fraction rate of oxygen is represented in Figures 4 to 9. These figures show only the near-field of the flow and the corresponding domain extends over 12 diameters along  $x$  and 3 diameters along  $y$ . The times corresponding to these figures are 11.75 ms for the figure 4, 12.4 ms for the figure 5, 13.06 ms for the figure 6, 13.71 ms for the figure 7, 14.36 ms for the figure 8 and 15.02 ms for the figure 9. The visualizations put in evidence a high unsteadiness of this flow which is involved by the shearing occurring in the inner mixing layer located between the two jets. The shearing involves the presence of large scale vortices attested by the high value of the time-averaged radial velocity (see Figure 3) in the near-field. A previous numerical study (see Reynier & Ha Minh 1996a) has established the coupling between the large scale vortices occurring in the inner mixing layer and the pulling out of the oxygen. This coupling between the pulling out of oxygen and the presence of coherent structures is in agreement with the atomization model proposed by Andrews (1993) where the destruction of the liquid core is involved by the presence of coherent structures at the liquid-gas interface. Here, the flow has not a high degree of organization notably after  $3D$ . This lack of organization can be explained by the high contrast of density between the two streams. The high level of instability involves a fast destruction of the core of oxygen. As the flow moves downstream the mixing becomes more and more intense particularly after the destruction of the oxygen core at approximately  $2D$ . This high mixing involves the pulling out of the oxygen in the shape of filaments then the tearing of these filaments. The mechanism of destruction of the oxygen core is involved by the vortices dominating the inner mixing layer. They involve the formation of filaments but also the tearing of oxygen packets along  $x$  on the axis. The de-

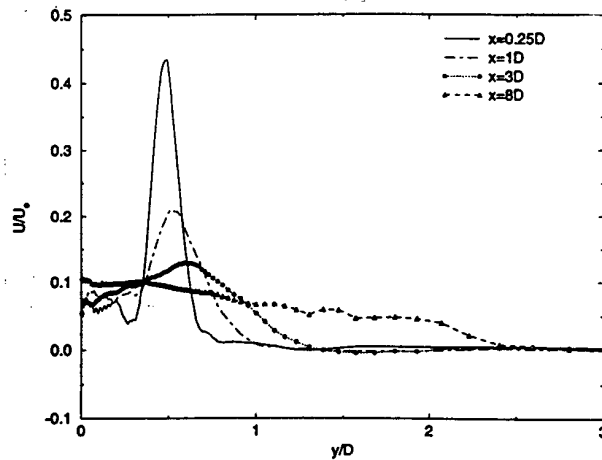


Figure 2: Time-averaged profiles of streamwise velocity

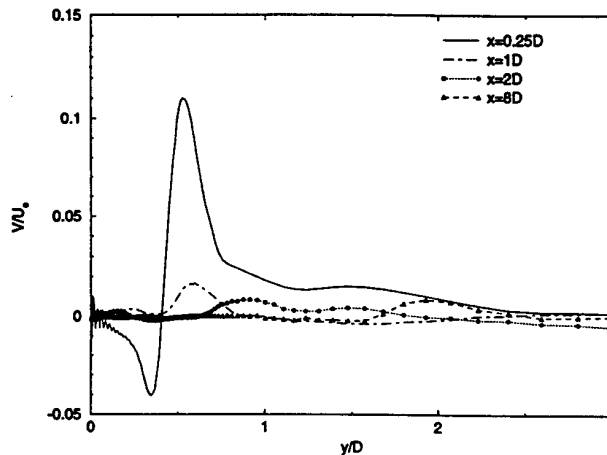


Figure 3: Time-averaged profiles of radial velocity

tachment of the oxygen packets occurs at approximately  $2D$ , then they are destroyed as they move downstream. This phenomenon of destruction of the oxygen core is very violent. This agrees qualitatively with the experiment of Rupe (1962) who observed that laminar flows can be more unstable and are atomized in a more violent fashion than fully-developed turbulent jets, due to higher radial velocity.

## CONCLUSION

In a previous numerical study (see Reynier & Ha Minh 1996a) turbulence models have been applied to the simulation of natural coherent unsteadiness in heterogeneous coaxial jets. These previous results showed that the large scale structures evolving in the flow are at the source of the pulling out of the oxygen by the hydrogen stream. Here, the direct simulation of heterogeneous jets confirms this point. The simulation of the destruction process of the oxygen jet is very violent. This result is in qualitative agreement with past experiments. To precise this process and to approach the real flow which is a two-phase one, with a better reliability, three-dimensional calculations will be necessary.

## ACKNOWLEDGEMENTS

We are grateful to the CNES which support this work under the post-doctorate grant of P. Reynier.

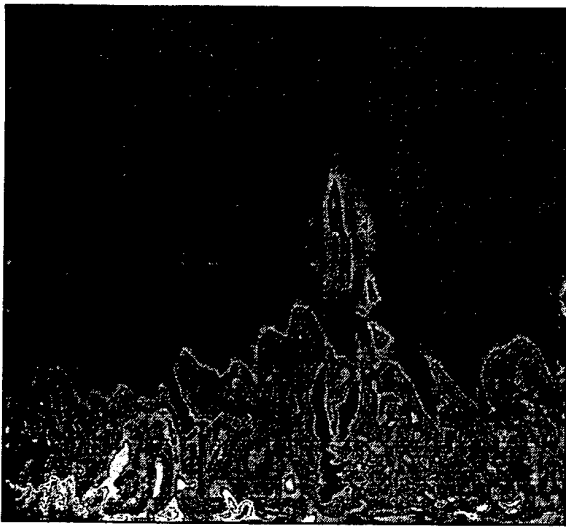


Figure 4: Unsteady field of mass fraction rate of oxygen at  $t=11.75$  ms

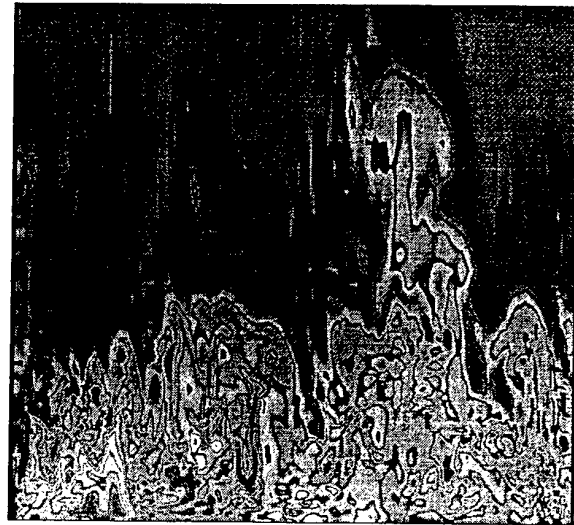


Figure 7: Unsteady field of mass fraction rate of oxygen at  $t=13.71$  ms

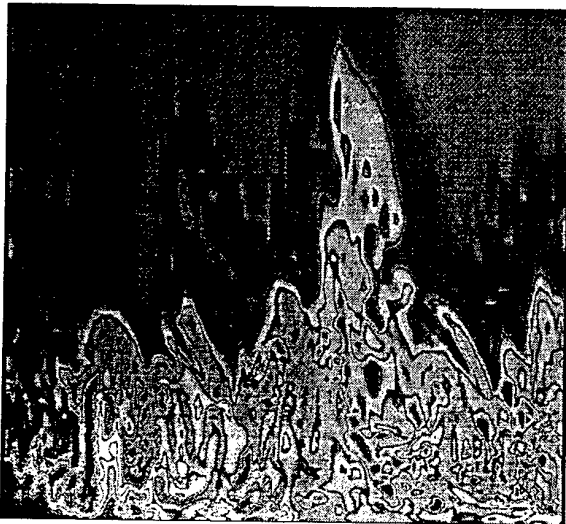


Figure 5: Unsteady field of mass fraction rate of oxygen at  $t=12.4$  ms



Figure 8: Unsteady field of mass fraction rate of oxygen at  $t=14.36$  ms

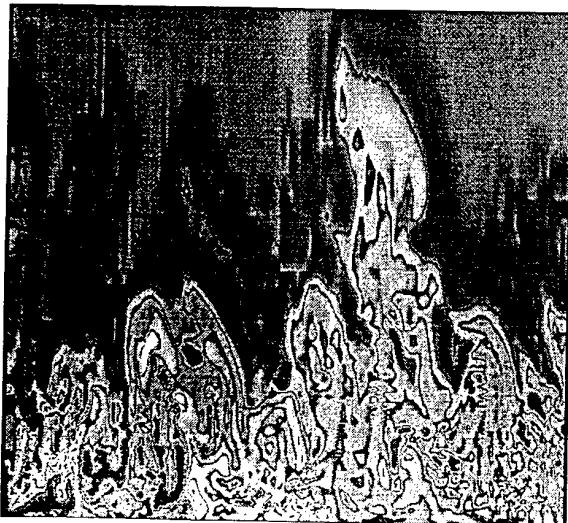


Figure 6: Unsteady field of mass fraction rate of oxygen at  $t=13.06$  ms

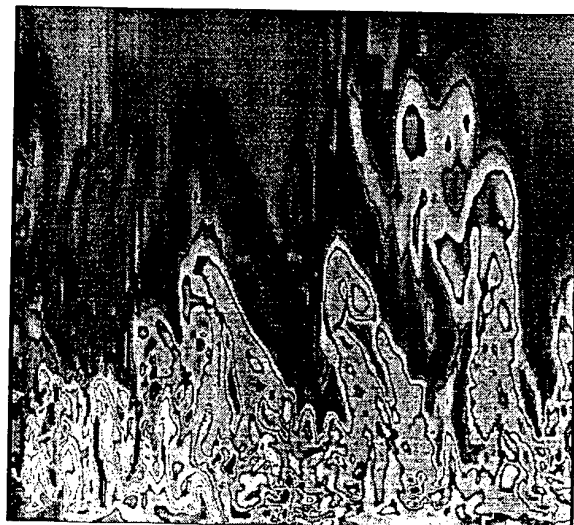


Figure 9: Unsteady field of mass fraction rate of oxygen at  $t=15.02$  ms

## REFERENCES

- Andrews, M. J., 1993, "The large-scale fragmentation of the intact liquid core of a spray jet", *Atomization and Sprays*, Vol. 3, pp. 29-54.
- Dahm, W. J. A., Frieler, C. E. and Tryggvason, G., 1992, "Vortex structure and dynamics in the near field of a coaxial jet", *J. Fluid Mech.*, Vol. 241, pp. 371-402.
- Gicquel, P., Vingert, L. & Brisson, E., 1995, "Caractérisation expérimentale d'un brouillard LOX-GH2 issu d'un injecteur coaxial en combustion", *Note Onera*.
- Gladnick, P. G., Enotiadis, A. C., Larue, J. C. and Samuelsen, G. S., 1990, "Near-field characteristics of a turbulent coflowing jet", *AIAA J.*, Vol. 28, pp. 1405-1414.
- Ha Minh, H. & Kourta, A., 1993, "Semi-deterministic turbulence modelling for flows dominated by strong organized structures", *9<sup>th</sup> Symp. Turb. Shear Flows*, Kyoto.
- Ingebo, R. D., 1992, "Effect of gas mass flux on cryogenic liquid jet breakup", *Cryogenics*, Vol. 32, pp. 191-193.
- Issac, K., Missoum, A., Drallmeier, J. & Johnston, A., 1994, "Atomization experiments in a coaxial coflowing Mach 1.5 flow", *AIAA J.*, Vol. 32, pp. 1640-1646.
- Lefebvre, A. H., 1992, "Energy considerations in twin-fluid atomization", *J. of Engineering for Gas Turbines and Power*, Vol. 114, pp. 89-96.
- MacCormack, R.W., 1981, "A numerical method for solving the equations of compressible viscous flow", *AIAA Paper 81-0110*.
- Mayer, W. O. H., 1994, "Coaxial atomization of a round liquid jet in a high speed gas stream: A phenomenological study", *Experiments in Fluids*, Vol. 16, pp. 401-410.
- Reynier, P. & Ha Minh, H., 1996a, "Influence of density contrast on instability and mixing in coaxial jets", *IUTAM Symp. on Variable Density Low Speed Turbulent Flows*, Marseille.
- Reynier, P. & Ha Minh, H., 1996b, "Numerical prediction of unsteady compressible turbulent coaxial jets", *Computers and Fluids*, accepted.
- Rupe, J. H., 1962, "On the dynamics characteristics of free liquid jets and a partial correlation with orifice geometry", *NASA Technical Report n° 32*.
- Tang, S. K. and Ko, N. W. M., 1994, "Coherent structure interactions in an unexcited coaxial jet", *Experiments in Fluids*, Vol. 17, pp. 147-157.
- Thompson, K. W., 1987, "Time dependent boundary conditions for hyperbolic systems", *J. Computational Physics*, Vol. 68, pp. 1-24.
- Tsai, S. C. & Viers, B., 1992, "Airblast atomization of viscous newtonian liquids using twin-fluid jet atomizers of various designs", *J. Fluids Engineering*, Vol. 114, pp. 113-118.
- Wu, P. K. & Faeth, G. M., 1995, "Onset and end of drop formation along the surface of turbulent liquid jets in still gases", *Phys. Fluids*, Vol. 7, pp. 2915-2917.
- Wu, P. K., Tseng, L. K. & Faeth, G. M., 1992, "Primary breakup in gas/liquid mixing layers for turbulent liquids", *Atomization and Sprays*, Vol. 2, pp. 295-317.

# AMPLIFICATION AND REDUCTION OF TURBULENCE IN A HEATED JET/SHOCK INTERACTION

L. JACQUIN & P. GEFFROY

Direction de l'Aérodynamique  
Office National d'Etudes et de Recherches Aérospatiales  
29, Avenue de la Division Leclerc  
92320 Châtillon - France

## ABSTRACT

This paper presents an experimental study on the interaction of a heated jet with a normal shock wave in a Mach 1.6 nozzle. The jet is heated to maintain a uniform Mach number ahead of the shock wave. The jump in the TKE across the shock is studied by means of 2D-LDV measurements. Turbulence in the central part of the jet is amplified. Amplification factors are close to those predicted by the linear theory and do not depend on the jet temperature. In the mixing layer, the jump in the turbulence properties are strongly dependent on the jet temperature. This seems to be primarily due to changes in the mean shear across the shock. These results are discussed in the light of available theoretical results in the field.

## INTRODUCTION

The problem of turbulence-shock wave interaction is an important topic for transonic and supersonic aeronautics. Two most important basic types of flows in the domain are shock/boundary layer interactions and under-expanded supersonic jets. Only shock/boundary layer interactions have been widely studied (see Détery & Marvin, 1986, for a review).

In the past ten years, a renewal of interest in this field has been motivated by projects relating to high capacity supersonic transportation. The problem has been revisited on a more fundamental basis. In particular, the case of homogeneous turbulence, which is propitious to theoretical, numerical and experimental developments, has been investigated. Experiments, direct numerical simulations and linear theory have brought a deeper comprehension of the way a shock wave transforms incoming homogeneous turbulence (see e.g. Lele, 1994 for a review). A unified phenomenology is not yet available, but several elements of the puzzle are now understood :

i) Results of turbulence amplification by a shock wave are mediated by compressible mechanisms which correspond to rapid exchanges between potential and kinetic energy in the nearfield behind the shock surface. Experimental investigation of these mechanisms by conventional means (LDV and hot wire) is a difficult task. They are described by the "linear interaction analysis" (LIA) developed by Ribner in the early fifties (see Ribner, 1953) and have been well characterised by direct numerical simulation (see Lele, 1994, for a review).

ii) Compressible mechanisms make the interaction between solenoidal isotropic homogeneous turbulence and a shock wave less energetic than a rapid one-dimensional compression of similar strength (see Lee et al., 1991, Jacquin et al., 1993(a)).

iii) As shown by linear theory and DNS, the issue of a turbulence/shock interaction depends on anisotropy of the upstream turbulence (see Mahesh et al., 1993) and on the thermodynamic properties of the upstream fluctuating fields

(Ribner, 1953, Moore, 1954, Hannapel & Friedrich, 1995, Mahesh et al. 1995, 1996). Concerning the last problem, recent theoretical and numerical results have shown that upstream entropy fluctuations may have a large influence on the interaction (Mahesh et al., 1997). This will be especially addressed in the present paper.

The question is whether these results will help to explain complex flows. For instance, in shock/boundary layer interaction, amplification of turbulent kinetic energy (TKE) is usually stronger than that predicted by linear analysis of homogeneous turbulence. Several mechanisms can promote turbulence in such a flow. First, the highest turbulence amplifications reported concern cases where the boundary layer separates in the shock region. In this case, turbulence amplification is mainly due to separation. This is not a direct effect of the shock itself. Moreover, when penetrating into the boundary layer, the shock induced compression is spread within a lambda shaped region. The resulting bulk compression may lead to higher amplification than that obtain behind a pure shock wave (see ii)). The anisotropy of the incoming turbulence and shock unsteadiness are other possible sources of amplification. Also, as shown by Mahesh et al. (1997), the thermodynamic equilibrium which prevails in an adiabatic boundary layer may promote amplification through baroclinic effects.

A new contribution to the field is presented here. It concerns the case of a heated jet interacting with a normal shock wave. This experiment aims at providing new results on the topic of free turbulent flow/shock interaction. Several arguments evoked above in the case of shock/boundary layer interaction will be discussed in the framework of this new study.

## EXPERIMENTAL SET-UP

The experimental set-up is shown in figure 1. A cylindrical sonic jet discharges into the sonic section of a  $M_0=1.6$  rectangular nozzle whose test section is  $120 \times 100 \text{ mm}^2$  (subscript 0 denotes the freestream, and j the jet flow). The jet exit diameter is  $D_j = 17 \text{ mm}$ . The exit static pressure of the jet is matched with that of the freestream. Consequently, the jet and the freestream expand together from  $M_j = M_{ext} = 1$  to Mach 1.6. Due to the change in the nozzle aspect ratio between the sonic throat and the test section, the jet becomes slightly elliptical. The Mach number being uniform across the jet, a pressure adapted interaction between the jet and a shock wave can be produced.

The velocity difference between the jet and the external flow is modulated by changing the jet temperature. An electric heater, of diameter  $33 \text{ mm}$ , located upstream of the ejector, is used for this purpose. Reduction in the diameter from this value to

$D_j = 17\text{mm}$  is made by means of a converging ejector (see figure 1). Three values of the total temperature ratio have been tested  $R_T = T_{ij}/T_{i\text{ext}} = 1, 2, 3$  ( $T_{i\text{ext}} = 300\text{K}$ ).

A normal shock, controlled by a second throat, is placed in the diverging part of the nozzle at location  $x_c = 110\text{mm}$ . This corresponds to  $x_c/D_j = 6.5$ . Figure 2 shows a schlieren picture of the flow for  $R_T = 3$  ( $T_{ij} = 900\text{K}$ )<sup>1</sup>.

### MEAN FIELD

Figure 3 shows the evolution of the mean velocity along the jet axis for  $R_T = 3$ . The flow accelerates in the diverging part of the nozzle (from  $M_j = 1$  at  $x=0$  to  $M_j = 1.6$  at  $x=90\text{mm}$ ). Then the velocity of the jet decreases progressively as it develops. When the interaction with the shock wave occurs, the jet still possesses a « potential » core. Figure 3 also shows that just after the shock deceleration, the flow undergoes a slight reacceleration. This comes from the separation of the nozzle boundary layers. This phenomenon is visible on the Schlieren picture in figure 2.

Figure 4 shows the Mach number and the total temperature distributions. Measurements were obtained by means of pressure and thermocouple probes situated  $10\text{mm}$  upstream ( $x=100\text{mm}$ ) and downstream ( $x=120\text{mm}$ ) of the shock. The upstream part of the flow is characterized by a uniform Mach number distribution, except for a slight deficit in the mixing layer region due to the pressure loss in the jet generator boundary layer. The uniformity of the pressure and Mach number distributions are preserved across the shock. The photograph in figure 2 shows that the shock surface is not distorted by the jet.

In the present flow, there are variations of the mean shear in the diverging part of the nozzle as well as through the shock. This will influence the property of turbulence inside the mixing layer. These variations may be evaluated by considering the vorticity equation :

$$\frac{d\vec{\omega}}{dt} = \vec{\omega} \cdot \nabla \vec{u} - \vec{\omega} \text{div} \vec{u} + \frac{1}{\rho^2} \vec{\nabla} \rho \times \vec{\nabla} p \quad (1)$$

in the case of a one unidirectional compressible shear flow, such that :

$$\begin{cases} \vec{\omega} = (0, \Omega(x), 0), \vec{u} = (U(x, z), 0, 0) \\ p = p(x), \rho = \rho(x, z), M = M(x) \end{cases} \quad (2)$$

By combining (1) and (2) and expressing the baroclinic term by means of Euler and state equations, the solution of (1) can be easily written as :

$$\frac{\partial}{\partial x} \left( \frac{\Omega}{U} \right) = 0 \quad (3)$$

Consequently, the mean shear in the jet mixing layer,  $\Omega = \frac{\partial U}{\partial z}$ , increases in the diverging part of the nozzle and decreases through the shock wave<sup>2</sup>. If one discards entropy effects, these variations only depend on the Mach number distribution. From the sonic section to the shock location (where  $M \approx 1.6$ ), it is found that the mean shear increases by a factor 1.8 (this value is only indicative because the spreading of the mixing layer is not accounted for in this model). Note that the cylindrical shear

layer which hits the shock wave is not in equilibrium. It corresponds to the initial development region of a jet and, moreover, it is accelerated by the nozzle. Through the shock wave, one obtains :

$$\frac{\Omega_1}{\Omega_0} = \frac{U_1}{U_0} = C(M_0) = \frac{2 + (\gamma - 1)M_0^2}{(\gamma + 1)M_0^2} \quad (4)$$

where subscript 0 denotes flow conditions ahead of the shock, and subscript 1, those behind. For  $M_0 = 1.6$ ,  $\Omega_1/\Omega_0 = 0.49$  : the mean shear is reduced by nearly a factor 2. One can expect that this change in the mean shear across the shock will lead to a reduction of turbulence in the downstream part of the flow.

Finally, since the Mach number is uniform across the flow, the velocity ratio  $R_U = U_{\text{ext}}/U_j$ , the density ratio  $R_\rho = \rho_j/\rho_{\text{ext}}$  and the convective Mach number  $M_c$  of the jet mixing layer only depend on the total temperature ratio  $R_T = T_{ij}/T_{i\text{ext}}$  and on the Mach number :

$$R_U = R_T^{-1/2}, R_\rho = R_T^{-1}, M_c = M \frac{R_T^{1/2} - 1}{R_T^{1/2} + 1} \quad (1)$$

with  $M = M_j = M_{\text{ext}}$ . When  $M = 1.6$ , this gives :

$R_T$	$R_\rho$	$R_U$	$M_c$
1	1	1	0
2	0.5	0.71	0.27
3	0.33	0.58	0.42

Table 1 : Mixing parameters for  $M = 1.6$

$M_c$  does not exceed 0.5 so that compressibility induced effects in the mixing layer are assumed to be weak.

### SECOND ORDER STATISTICS

Mean and fluctuating velocity components have been measured using a two-component LDV system. MgO particles were used for seeding the flow. The Reynolds stresses  $\overline{u'^2}$ ,  $\overline{w'^2}$  and  $\overline{u'w'}$  ( $w'$  is the vertical component of velocity) have been determined for the three jet temperatures, with and without shock wave. Vertical profiles measured ahead ( $x=100\text{mm}$ ) and downstream ( $x=110\text{mm}$ ) of the shock wave are drawn in figure 5. Figure 6 shows the corresponding amplification factors  $R_{u,2} = \overline{u_1'^2}/\overline{u_0'^2}$ ,

$R_{w,2} = \overline{w_1'^2}/\overline{w_0'^2}$  and  $R_{q,2} = q_1^2/q_0^2$  where  $q^2 = \overline{u'^2} + 2\overline{w'^2}$ .

In figure 5, it is observed that even though the mixing layer has not reached the jet axis at  $x=100\text{mm}$  ( $x/D_j = 6.5$ ), the central region of the jet is turbulent. This turbulence is created by the heating system located inside the jet generator and is locally quasi-homogeneous. The flow amounts to the superposition of a turbulent mixing layer and a quasi-homogeneous turbulence located in its centre. Figures 5 and 6 show that the issue of the shock interaction depends upon the region considered.

### Quasi homogeneous turbulence

In the jet axis region ( $-5\text{mm} \leq z \leq 5\text{mm}$ ) turbulence is amplified. Values of the energy components, the anisotropy ratio ( $\overline{u_0'^2}/\overline{w_0'^2}$ ), the upstream turbulence rate ( $q_0^2/U_0$ ) and the corresponding amplification factors obtained at  $z=0$  are reported in table 2.

<sup>1</sup> Turbulence visible outside the jet in the downstream part of the flow corresponds to the boundary layers that develop on the side windows.

<sup>2</sup> Note that in a one-dimensional compression of homogeneous shear flow, one has  $\Omega U = Cte$  (see Mahesh et al. 1994). This corresponds to an inverse evolution with respect to equation (3). Consequently, homogeneous linear theory is not very useful for the interpretation of the jet mixing layer behavior in the present experiment.

$\overline{u'^2}$  is amplified whereas  $\overline{w'^2}$  is weakly affected. It is remarkable to note the invariance of  $R_2 = \overline{u'^2}/\overline{u_0'^2}$  with respect to  $R_T$ . The value obtained is very close to that given by the linear theory (LIA) (for initial solenoidal isotropic turbulence).

$R_T$	$\overline{u_0'^2}$ ( $m^2 s^{-2}$ )	$\overline{w_0'^2}$ ( $m^2 s^{-2}$ )	$\overline{u_0'^2}/\overline{w_0'^2}$	$U_0$ ( $ms^{-1}$ )	$q_0/U_0$	$\overline{u_1'^2}/\overline{u_0'^2}$	$\overline{w_1'^2}/\overline{w_0'^2}$	$\overline{u_1'^2}/\overline{w_1'^2}$	$q_1^2/q_0^2$
1	166	235	0.71	455	0.055	1.67	1.0	1.18	1.17
2	433	450	0.96	640	0.057	1.72	1.0	1.65	1.23
3	625	590	1.06	770	0.055	1.67	1.1	1.50	1.35

Table 2 : Turbulence properties on the jet axis ahead (subscript 0,  $x=100$  mm) and behind (subscript 1,  $x=120$  mm) the shock.

However, LIA predicts a slight increase in  $\overline{w'^2}$  which is not observed. Variation in the TKE amplification factor  $R_q = q_1^2/q_0^2$  mainly reflects changes in the initial anisotropy ratio  $\overline{u_0'^2}/\overline{w_0'^2}$ <sup>3</sup>. It may be noted in table 2 that the initial

turbulence rate  $\frac{q_0}{U_0}$  is constant. The upstream TKE value  $q_0$  thus increases by a factor  $\sim \sqrt{3}$  from  $R_T=1$  to 3. This does not seem to have a significant influence.

On the whole, one may conclude that in the central region of the jet, quasi-homogeneous turbulence is subjected to a moderate amplification and that the level of this amplification is compatible with linear theory. It does not seem to depend neither on the total temperature of the flow nor on the initial turbulence level.

#### Mixing layer

As shown in figures 5 and 6, changes in the turbulent quantities in the mixing layer are multiform.

For  $R_T = 1$ , turbulence in the wake region almost behaves like that in the central region :  $\overline{u'^2}$  is amplified, whereas  $\overline{w'^2}$  is almost unaffected, as well as  $\overline{u'w'}$ . In figure 6, there is no significant change in the amplification factors for  $R_T = 1$ , except in the external region of the jet ( $|z| > 11$  mm) where they increase. An increase in the external region is also observed for the two other temperature cases. It is provoked by a slight thickening of the jet behind the shock combined with the low levels of initial turbulence that prevails in this region.

For  $R_T \neq 1$ , changes in the mixing layer are characterized by a decrease of the shear stress  $\overline{u'w'}$ , an increase of  $\overline{w'^2}$  and by a

spectacular reduction of  $\overline{u'^2}$ . Interpretation of these results is not straightforward. Several mechanisms must be accounted for. The first one is the reduction in the mean shear across the shock. The second is possible temperature effects. The third concerns possible measurement bias due to LDV particle dynamics.

As shown above, the mean shear is reduced by a factor of two across the shock. This means that turbulence production is reduced in the same proportion. The shock wave transforms the supersonic mixing layer into a subsonic one which is less energetic but which contains intense turbulent fluctuations which results from the shock interaction. Consequently, a region exists downstream of the shock where this turbulence must be dissipated in order to match new equilibrium conditions.

One can try to characterize the above mechanisms by considering the normalised Reynolds stresses

$\sigma_u/\Delta U$ ,  $\sigma_w/\Delta U$ ,  $\sigma_u/\sigma_w$  and  $\overline{u'w'}/q^2$  where  $\sigma$  denotes a

r.m.s (e.g.  $\sigma_u = \sqrt{\overline{u'^2}}$ ) and  $\Delta U$ , the difference in the mean velocity across the mixing layer ( $\Delta U = U_{axis} - U_{ext}$ ;  $\Delta U$  varies according to (3) :  $\Delta U/U = Cte$ ). Figure 7 shows the evolution of these quantities along a line connecting points where  $q^2$  is maximum. We focus on the region  $70mm \leq x(mm) \leq 150mm$  between the nozzle acceleration and the development region of the jet.

In the supersonic regime, ahead of the shock, one obtains  $\sigma_u/\Delta U \approx 0.2$ ,  $\sigma_w/\Delta U \approx 0.1$  and  $\overline{u'w'}/q^2 \approx 0.19$  for  $R_T=3$ . A slightly higher value of  $\sigma_w/\Delta U$  is obtained for  $R_T=2$ . For the anisotropy ratio, one obtains  $\sigma_u/\sigma_w = 1.9$  for  $R_T=3$  and 1.7 for  $R_T=2$ . Experiments on plane supersonic mixing layers at moderate convective Mach numbers suggest smaller values for  $\sigma_u/\Delta U$  ( $\approx 0.175$ ), and similar values for  $\sigma_w/\Delta U$  (see a review in Smits & Dussauge, 1996). Consequently, the anisotropy ratio of the supersonic upstream in the present experiment are higher than that commonly observed.

The normalised components of energy increases behind the shock<sup>4</sup> and the anisotropy is decreased to a more standard value of 1.3. It is striking to note that, compared to results on equilibrium plane mixing layer, the flow at  $x=150mm$  is characterised by higher values of the normalised components of energy but by a more conventional value of the anisotropy ratio. As discussed by Jacquin et al. 1995, high values of the anisotropy ratio have been already observed in LDV measurements in supersonic heated jets, but also in plane mixing layers. As explained by these authors, seeding bias could contribute to this behaviour. If any, these bias should depend on the mean shear amplitude. This could explain why the anisotropy ratio increases upstream with  $R_T$  and why it decrease suddenly in the subsonic regime behind the shock. This problem is the object of ongoing research.

As seen through the behaviour of the normalised TKE production ( $\overline{u'w'}/q^2$ ) adaptation of the flow to downstream conditions takes place at a distance of 20 or 30mm. A characteristic distance for the dissipation can be evaluated as

<sup>3</sup> As explain above, the turbulence in the jet's central region is produced inside the jet generator. It is subjected to an axisymmetric compression inside the sonic ejector and to an axisymmetric expansion inside the tunnel nozzle. The first effect leads to a strong decrease of the anisotropic ratio  $\overline{u'^2}/\overline{w'^2}$ , the second, to an increase. The values of  $\overline{u_0'^2}/\overline{w_0'^2}$  obtained at the shock level results from the combination of these mechanisms. This depends on the jet velocity, that is on the jet temperature.

<sup>4</sup>  $\sigma_u/\Delta U$  is subjected to a sharp overshoot at the shock level. This overshoot is commonly observed in LDV results. It is due to a combination of the shock intermittency and particle drag effects (differences in the dynamic response of particles of various sizes to the shock induced deceleration). The amplitude and the thickness of this spurious "particle drag turbulence" is enhanced by shock unsteadiness (see Jacquin et al. 1993(b) for further details).



$(\Delta x)_\varepsilon = U \tau_\varepsilon$  where  $U$  denotes the convection velocity and  $\tau_\varepsilon = (q^2/2)/\varepsilon$  the dissipation time scale, with  $\varepsilon$  the TKE dissipation rate. The time scale ( $\tau_\varepsilon$ ) can be only evaluated ahead of the shock if equilibrium between production and dissipation is assumed. The dissipation rate ( $\varepsilon_0$ ) then reads:  $\varepsilon_0 = (\overline{u'w'}\partial U/\partial z)_0$ . The change in the time scale  $\tau_\varepsilon = (q^2/2)/\varepsilon$  through the shock is unknown. Assuming that  $\tau_\varepsilon$  is conserved<sup>5</sup>, that is  $\tau_{\varepsilon 1} = \tau_{\varepsilon 0} = (q_0^2/2)/\varepsilon_0$ , using the maximum values of  $\overline{u'w'}$  and  $\partial U/\partial z$  at  $x=100\text{mm}$  and the velocity  $U_1$  measured downstream in the mixing layer, one obtains  $(\Delta x)_{\varepsilon 1} = U_1 \tau_{\varepsilon 0} \approx 60\text{mm}$  for  $R_T = 2$  and  $(\Delta x)_{\varepsilon 1} \approx 40\text{mm}$  for  $R_T = 3$ , respectively. These values are equivalent to those observed. This confirms that turbulence of the mixing layer is subjected to rapid dissipation behind the shock. However, as shown in figure 7, properties of the downstream mixing layer strongly differ from those upstream. This behavior is not yet understood.

### ABOUT TEMPERATURE EFFECTS

As previously stated, a theoretical analysis of the behaviour of the fluctuating field across the shock may be done in the framework of Ribner's linear interaction analysis (LIA). Ribner (1953) developed the case of upstream pure shear waves. This analysis has been recently extended by Mahesh et al. (1996) to cases where additional entropy waves are present (see also Mahesh et al., 1997). In the latter case, the theory shows that the correlation between the vorticity and the entropy fluctuations strongly influences the evolution of turbulence across the shock. In particular, Mahesh et al. have shown that a negative temperature-velocity correlation  $\overline{u'T}$  upstream of the shock enhances TKE amplification; whereas if  $\overline{u'T}$  is positive the amplification is strongly damped.

Considering the homogeneous region of the flow, one may assume that correlation between velocity and temperature is not promoted by increase in the mean total temperature of the flow. This is consistent with an invariance of the amplification factors with respect to  $R_T$  as observed in figure 6.

Contrarily, temperature effects may be present in the mixing layer. The mean temperature gradient across the mixing layer is aligned with the mean velocity gradient, so that strong positive  $\overline{u'T}$  must prevail<sup>6</sup>. Thus baroclinic effects could contribute to lessen the TKE amplification in the mixing layer. Unfortunately, this effect cannot be isolated from the consequences of the mean shear reduction. One can however note in figure 7 a slight reduction in the downstream TKE as  $R_T$  increases.

<sup>5</sup> Actually, DNS and experiments on homogeneous turbulence show that the shock compression leads an augmentation of enstrophy (see work by Lele et col. and Jacquin et al., 1993(b)). This must lead to an increase of  $\tau_\varepsilon$ .

<sup>6</sup> A fluid particle displaced impulsively from the free flow into the jet flow possesses a negative velocity fluctuation,  $u'$ , and a negative temperature fluctuation  $T'$ ; both fluctuations are positive in the opposite case.

### SUMMARY

An experiment is presented in which a heated jet interacted with a normal shock wave. A pressure matched interaction with a nearly uniform Mach number distribution ahead and behind the shock wave was obtained by heating the jet. The turbulent properties of this interaction were measured by LDV. The following trends have been observed :

- 1) The present flow is characterised by two types of turbulence. The first is a quasi-homogeneous turbulence convected in the central region of the jet. The second is that which develops in the mixing layer.
- 2) The quasi-homogeneous turbulence prevailing in the central part of the flow is amplified at a rate which corresponds to the linear theory prediction. Amplification is not significantly affected by temperature nor by the upstream turbulence intensity.
- 3) The reduction in the mean shear which is induced by the shock wave leads to a decrease in the turbulence activity of the subsonic mixing layer downstream of the shock. Accordingly, a reduction in the TKE may be found through the shock in the mixing layer.
- 4) Individual components of the TKE measured upstream of the shock are characterized by a significant departure from equilibrium. Equilibrium is never reached downstream of the shock, perhaps because of the jet development.
- 5) As suggested in Mahesh et al. (1997), baroclinic effects could participate in the reduction of the TKE amplification in the shear layer. Unfortunately, this cannot be corroborated in the present experiment because the flow behind the shock is dominated by rapid changes in the TKE production and by a rapid dissipation.
- 6) On the whole, this jet/shock interaction is characterized by TKE amplifications smaller than those observed in other flows where shock-induced distortions are present, as in shock/boundary layer interactions or in under-expanded jets.

### Acknowledgement

This research has been supported by the Direction des Recherches et Etudes Techniques of the French Ministry of Defense.

### REFERENCES

- Délery J. & Marvin J.G., 1986, "Turbulent shock/boundary layer interaction", AGARDograph 280.
- Smits A.J. & Dussauge J.P., 1996, "Turbulent shear layers in supersonic flows", AIP Press.
- Lele S.K., 1994, "Compressibility effects on turbulence", *Ann. Rev. Fluid Mech.* **26**, pp 211-254.
- Ribner H.S., 1953, "Convection of a pattern of vorticity through a shock wave". Lewis Flight Propulsion Laboratory. RP 1164.
- Lee S., Lele S.K. & Moin P., 1991, "Direct numerical simulation and analysis of shock turbulence interaction". AIAA Paper 91-0523.
- Moore F.K., 1954, "Unsteady oblique interaction of a shock wave with a plane disturbance", Lewis Flight Propulsion Laboratory. RP 1165.
- Hannappel R. & Friedrich R., 1995, "Interaction of isotropic turbulence with a normal shock-wave", *Appl.Sci. Res.*, **54**, 205-221.
- Mahesh K., Lele S.K. & Moin P., 1993, "The response of anisotropic turbulence to rapid homogeneous one-dimensional compression", *Phys. Fluids* **6**, 1052-1062.

Mahesh K., Lee S., Lele S.K. & Moin P., 1995, " The interaction of an isotropic field of acoustic waves with a shock wave ", *J. Fluid Mech.* 300, 383-407.

Jacquin L., Cambon C. & Blin E., 1993(a), "Turbulence amplification by a shock wave and rapid distortion theory", *Phys. Fluids A* 5 (10), pp 2539-2550.

Jacquin L., Blin E. & Geffroy P., 1993(b), "An experiment on free turbulence/shock wave interaction", *Turbulent Shear Flows* 8, Springer-Verlag, Berlin, pp 229-248.

Mahesh K., Lele S. & Moin P., 1996, " The interaction of a shock wave with a turbulent shear flow". Report TF.69, Thermosciences Division, Mechanical Engineering Department, Stanford University, Stanford California.

Mahesh K., Lele S. & Moin P., 1997, " The influence of entropy fluctuations on the interaction of turbulence with a shock wave », to appear in the *J. Fluid. Mech.*

Jacquin L., Mistral S., Geffroy P. & Cruaud F., 1995, "Mixing of a heated supersonic jet with a supersonic parallel stream", *Advances in Turbulence V*, Springer-Verlag, 1995.

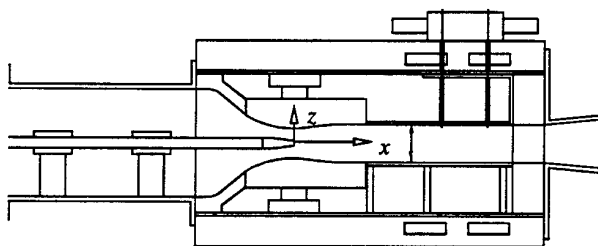


Figure 1 : Experimental set-up

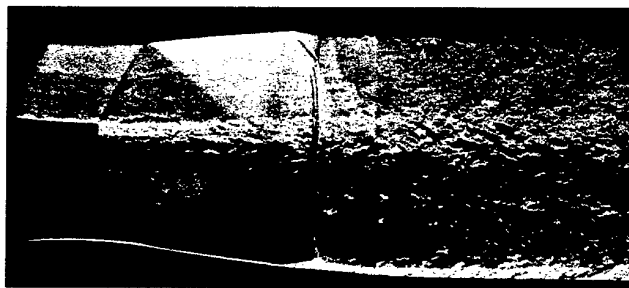


Figure 2 : Schlieren picture (20 ns) of the flow

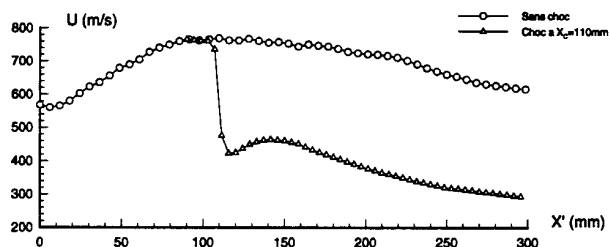


Figure 3 : Evolution of the mean velocity along the jet axis for the case  $R_T = 3$ .

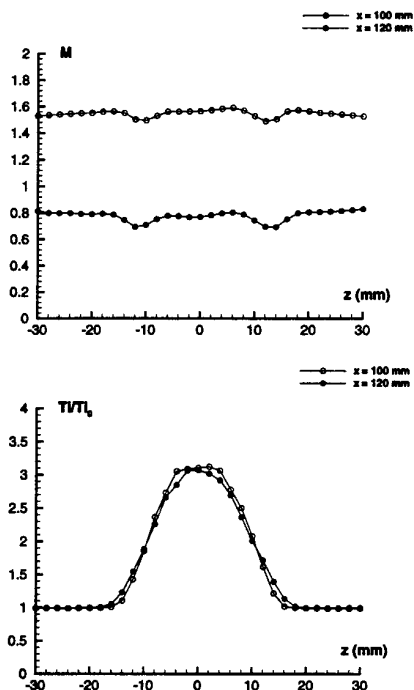
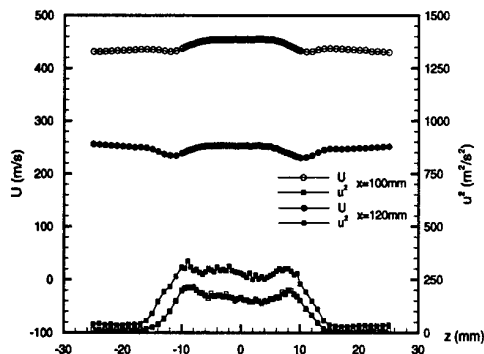
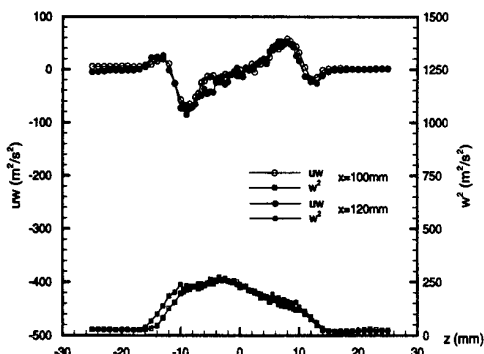


Figure 4 : Mach number and total temperature distribution at  $x=100\text{mm}$  and  $120\text{ mm}$  for the case  $R_T = 3$



(a)



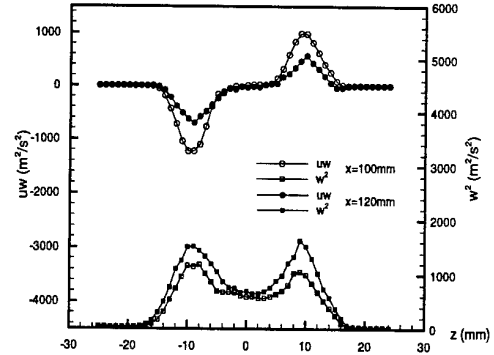
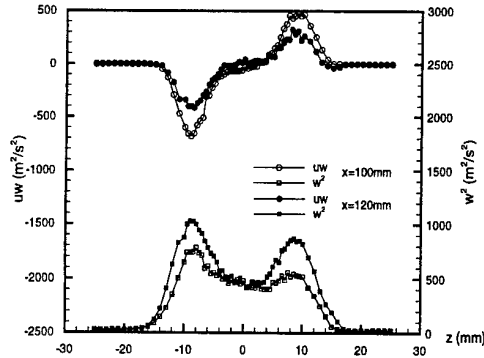
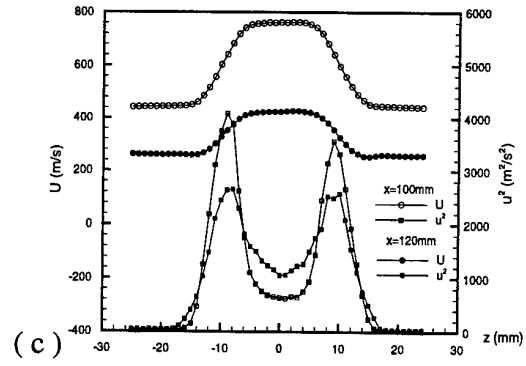
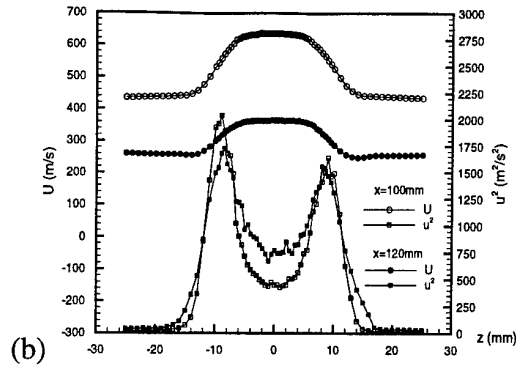


Figure 5 : Vertical profiles of  $U$  and of the Reynolds stresses upstream and downstream from the shock wave. (a), (b), (c)  $R_T=3$ .

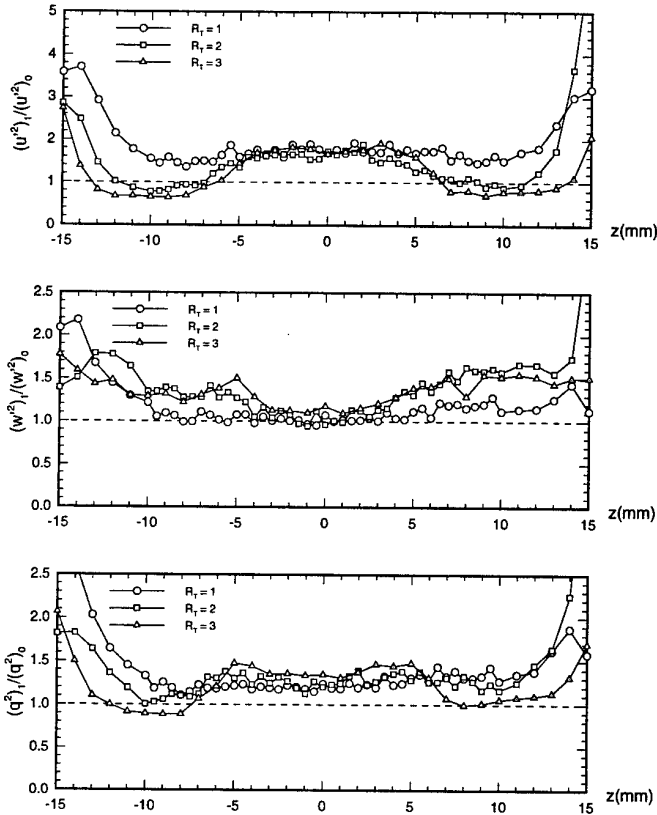


Figure 6 : Amplification factors  $R_{u,2} = \overline{u_1'^2} / \overline{u_0'^2}$ ,  $R_{w,2} = \overline{w_1'^2} / \overline{w_0'^2}$   
 $R_{q,2} = q_1^2 / q_0^2$  (subscript 1 :  $x=120\text{mm}$ , subscript 0 :  $x=100\text{mm}$ ) for  
 $R_T = 1, 2, 3$ .

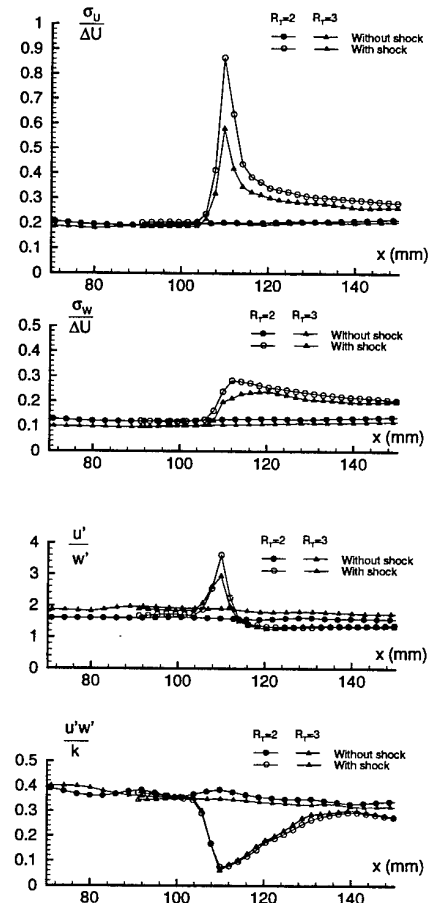


Figure 7 : Evolution of the normalized Reynolds stresses in the mixing layer for  $R_T = 2$  and 3.